Self-sorting of nonmuscle myosins IIA and IIB polarizes the cytoskeleton and modulates cell motility

Maria S. Shutova,[1] Sreeja B. Asokan,[3] Shefali Talwar,[2] Richard K. Assoian,[2] James E. Bear,[3] and Tatyana M. Svitkina[1]

[1]Department of Biology and [2]Department of Systems Pharmacology and Translational Therapeutics, University of Pennsylvania, Philadelphia, PA
[3]Department of Cell Biology and Physiology, UNC Lineberger Comprehensive Cancer Center, University of North Carolina at Chapel Hill, Chapel Hill, NC

Nonmuscle myosin II (NMII) is uniquely responsible for cell contractility and thus defines multiple aspects of cell behavior. To generate contraction, NMII molecules polymerize into bipolar minifilaments. Different NMII paralogs are often co-expressed in cells and can copolymerize, suggesting that they may cooperate to facilitate cell motility. However, whether such cooperation exists and how it may work remain unknown. We show that copolymerization of NMIIA and NMIIB followed by their differential turnover leads to self-sorting of NMIIA and NMIIB along the front–rear axis, thus producing a polarized actin–NMII cytoskeleton. Stress fibers newly formed near the leading edge are enriched in NMIIA, but over time, they become progressively enriched with NMIIB because of faster NMIIA turnover. In combination with retrograde flow, this process results in posterior accumulation of more stable NMIIB-rich stress fibers, thus strengthening cell polarity. By copolymerizing with NMIIB, NMIIA accelerates the intrinsically slow NMIIB dynamics, thus increasing cell motility and traction and enabling chemotaxis.

Introduction

Nonmuscle myosin II (NMII) is one of the most abundant and ubiquitous proteins in cells. It is uniquely responsible for generation of contractile force in nonmuscle cells and is essential for directional cell motility, adhesion, and tissue morphogenesis, as well as cancer cell invasion and metastasis (Heissler and Manstein, 2013). Hexameric NMII molecules, each consisting of two heavy chains and two pairs of light chains, polymerize into bipolar filaments to cause contraction of actin–NMII bundles (stress fibers) and less organized actin–NMII networks (Heissler and Manstein, 2013). Through its contractile and cross-linking activities, NMII also plays a key role in organizing the stress fiber system, which coordinates motile activities across the cell. The organization of the stress fiber system varies greatly among cell types to match their different needs. This variability is typically achieved through different combinations of three major types of stress fibers (Small et al., 1998; Hotulainen and Lappalainen, 2006; Tojkander et al., 2012): ventral stress fibers located at the basal cell surface and typically anchored to the substrate by focal adhesions at both ends, radial (or dorsal) stress fibers that usually have a focal adhesion only at the distal end near the leading edge, and transverse arcs that lie parallel to and at some distance from the cell leading edge and often incorporate the proximal ends of radial stress fibers. How these different stress fibers are formed is an active area of research (Kovac et al., 2013; Burnette et al., 2014; Schulze et al., 2014; Soiné et al., 2015; Tojkander et al., 2015).

Mammals have three NMII paralogs (NMIIA, NMIIB, and NMIIC) that contain heavy chains encoded by the *MYH9*, *MYH10*, and *MYH14* genes, respectively. The NMII paralogs have different expression profiles and play both unique and overlapping roles in cells (Wang et al., 2011; Heissler and Manstein, 2013). NMIIA and NMIIB are widely expressed, whereas expression of NMIIC is more limited (Golomb et al., 2004). Despite extensive research addressing individual and collective roles of NMII paralogs in cells, it remains largely unclear at the conceptual level how the expression profile of NMII paralogs in individual cells is linked to cell physiology. The recent discovery that NMIIA and NMIIB can copolymerize in cells (Beach et al., 2014; Shutova et al., 2014), together with the distinct kinetic properties of the NMIIA and NMIIB motors (Kovács et al., 2007; Billington et al., 2013; Nagy et al., 2013; Heissler and Sellers, 2016) and differences in the NMIIA and NMIIB turnover rates (Sandquist and Means, 2008; Vicente-Manzanares et al., 2008; Raab et al., 2012), raises a possibility that cells may be able to tune their morphology, cytoskeletal organization, and/or migratory behavior through copolymerization of NMIIA and NMIIB at different ratios. In this study, we tested this possibility and revealed the underlying mechanism by which cells fine-tune cytoskeletal organization and cell motility through copolymerization of NMIIA and NMIIB.

We show that when NMIIA and NMIIB are expressed individually, they favor the formation of radial/transverse and ventral stress fibers, respectively, consistent with their kinetic and dynamic properties. However, when both paralogs are

Correspondence to Tatyana Svitkina: svitkina@sas.upenn.edu

Abbreviation used: NMII, nonmuscle myosin II.

The Rockefeller University Press
J. Cell Biol. Vol. 216 No. 9 2877–2889
https://doi.org/10.1083/jcb.201705167

present simultaneously, an increase in the relative NMIIA/NMIIB expression causes progressive redistribution of NMIIB to gradually adopt an NMIIA-like pattern through intermediate formation of a characteristic anterior–posterior NMIIA/NMIIB gradient at an optimal NMIIA/NMIIB ratio. Moreover, addition of NMIIA accelerates the intrinsically slow NMIIB dynamics and is necessary for cell migration, traction and chemotaxis. We also show that the polarized anterior–posterior NMIIA–NMIIB distribution is formed by a gradual replacement of NMIIA by NMIIB within individual stress fibers in the course of their retrograde flow. Based on these data, we propose a mechanistic model centered on copolymerization of NMII paralogs that explains how cells can tune their migratory behavior by using different combinations of NMIIA and NMIIB.

Results

NMIIB in the absence of NMIIA supports formation of discrete ventral stress fibers

REF-52 rat embryo fibroblasts endogenously express both NMIIA and NMIIB, but not NMIIC (Fig. 1 A). Spreading REF-52 cells formed an integrated system of actin–NMII bundles that was dominated by radial stress fibers and transverse arcs, whereas ventral stress fibers were rare (Fig. 1 B). NMIIA and NMIIB often were present simultaneously in the stress fibers, but at a different ratio. In general, the NMIIB distribution was shifted farther away from the cell edge relative to NMIIA (Fig. 1 B), as also reported for many other cell types (Maupin et al., 1994; Kelley et al., 1996; Kolega, 1998; Saitoh et al., 2001; Vicente-Manzanares et al., 2008).

Because of different biophysical properties and dynamic behavior, NMIIA and NMIIB may intrinsically favor assembly of different stress fiber types. To test this idea, we depleted either NMIIA or NMIIB from REF-52 cells using shRNA (Fig. 1 A). Whereas nontargeting shRNA had no effects on spreading REF-52 cells, after NMIIA knockdown, REF-52 cells lost most of their stress fibers, as also has been reported for other cells (Cai et al., 2006; Sandquist et al., 2006; Even-Ram et al., 2007; Betapudi, 2010). Importantly, there was also a qualitative change in stress fiber composition. The NMIIA-knockdown cells mostly contained only a few discrete ventral stress fibers (Fig. 1 C) attached to focal adhesions at both ends (Fig. 1 E) but lost the majority of their radial stress fibers and transverse arcs. NMIIA-knockdown cells often had less polarized morphology with lamellipodia distributed around the cell perimeter, even in fully spread cells. They were also thicker in the perinuclear area (6.8 ± 1.7 µm, mean ± SD, $n = 9$; $P < 0.01$) than control (4.8 ± 0.9 µm, $n = 11$) and NMIIB-depleted (4.7 ± 0.7 µm, $n = 11$) cells, consistent with the idea that transverse arcs contribute to cell flattening (Burnette et al., 2014). Knockdown of NMIIB in REF-52 cells did not result in obvious changes of stress fiber organization, so that the transverse arcs and radial stress fibers remain predominant stress fiber types (Fig. 1 D). However, NMIIB knockdown caused a significant reduction of the cell projection area (3,244 ± 1,065 µm^2, $n = 40$; $P < 0.001$; Dunn's multiple comparison test) compared with the control (5,249 ± 2,137 µm^2) and NMIIA knockdown (4,354 ± 1,504 µm^2) cell lines, suggesting that NMIIB may contribute to stabilization of cell spreading. A decrease in cell spreading after NMIIB knockdown was also observed in A549 cells (Sandquist et al., 2006).

Together, these results not only validate various aspects of previously reported phenotypes of NMIIA or NMIIB depletion in different cell types but also suggest that NMIIA and NMIIB favor formation of distinct stress fiber types. Thus, NMIIB in the absence of NMIIA supports the formation of discrete ventral stress fibers, whereas NMIIA promotes the assembly of an integrated stress fiber system dominated by transverse arcs and radial stress fibers.

Ectopic expression of NMIIA in COS-7 cells lacking endogenous NMIIA induces the formation of radial stress fibers and transverse arcs

COS-7 cells endogenously express NMIIB and NMIIC, but not NMIIA (Bao et al., 2005; Fig. 1 A). Organization of stress fibers in wild-type COS-7 cells (Fig. 2 A) closely resembled that of NMIIA-depleted REF-52 fibroblasts (Fig. 1 C). Specifically, COS-7 cells contained a few discrete NMIIB-positive ventral stress fibers that typically terminated in focal adhesions at both ends (Fig. 2 E). This observation supports the idea that NMIIB favors formation of ventral stress fibers.

We next tested whether ectopic expression of NMIIA would change the stress fiber organization in COS-7 cells (Fig. 2 C). To distinguish effects of an increase in total NMII levels from NMIIA-specific changes, we overexpressed GFP-NMIIB in wild-type COS-7 cells as a control (Fig. 2 B). Formation of different stress fiber types was quantified in cells with no/low, medium, or high expression of either GFP-NMIIA or GFP-NMIIB (Fig. 2 D). The number and connectivity of stress fibers was slightly higher in COS-7 cells overexpressing GFP-NMIIB than in wild-type cells (Fig. 2, B and D). However, these stress fibers still localized mostly at the ventral cell surface, had sharply defined linear contours, and were connected to focal adhesions at their ends, as is typical for ventral stress fibers (Fig. 2 E). In contrast, the majority of COS-7 cells expressing GFP-NMIIA developed a highly integrated network of radial stress fibers and transverse arcs (Fig. 2, C and D). These results from a different system further support the conclusion that NMIIB and NMIIA favor formation of ventral and radial/transverse stress fibers, respectively.

Ectopic expression of NMIIA in COS-7 cells causes progressive scattering of endogenous NMIIB

In addition to inducing transverse and radial stress fibers, overexpression of NMIIA in COS-7 cells also led to noticeably decreased formation of ventral stress fibers (Fig. 2 D), suggesting that the presence of NMIIA may influence NMIIB-mediated assembly of ventral stress fibers. To test this idea, we evaluated NMIIB localization in COS-7 cells expressing NMIIA (Fig. 3). Remarkably, the intracellular distribution of endogenous NMIIB in COS-7 cells was affected by the presence of GFP-NMIIA in an expression level–dependent manner (Fig. 3, A–C). At low levels of exogenous NMIIA, NMIIB did not noticeably change its intrinsic distribution and was present in a few sharply defined ventral stress fibers, and GFP-NMIIA largely colocalized with the endogenous NMIIB (Fig. 3 A). However, when GFP-NMIIA was expressed at high levels, endogenous NMIIB became uniformly dispersed throughout the cell in the form of small puncta (Fig. 3 C). At intermediate levels of GFP-NMIIA expression, endogenous NMIIB and exogenous NMIIA formed a characteristic front–rear gradient of NMIIA/NMIIB distribution (Fig. 3 B) similar to that observed in wild-type REF-52 cells (Fig. 1 A).

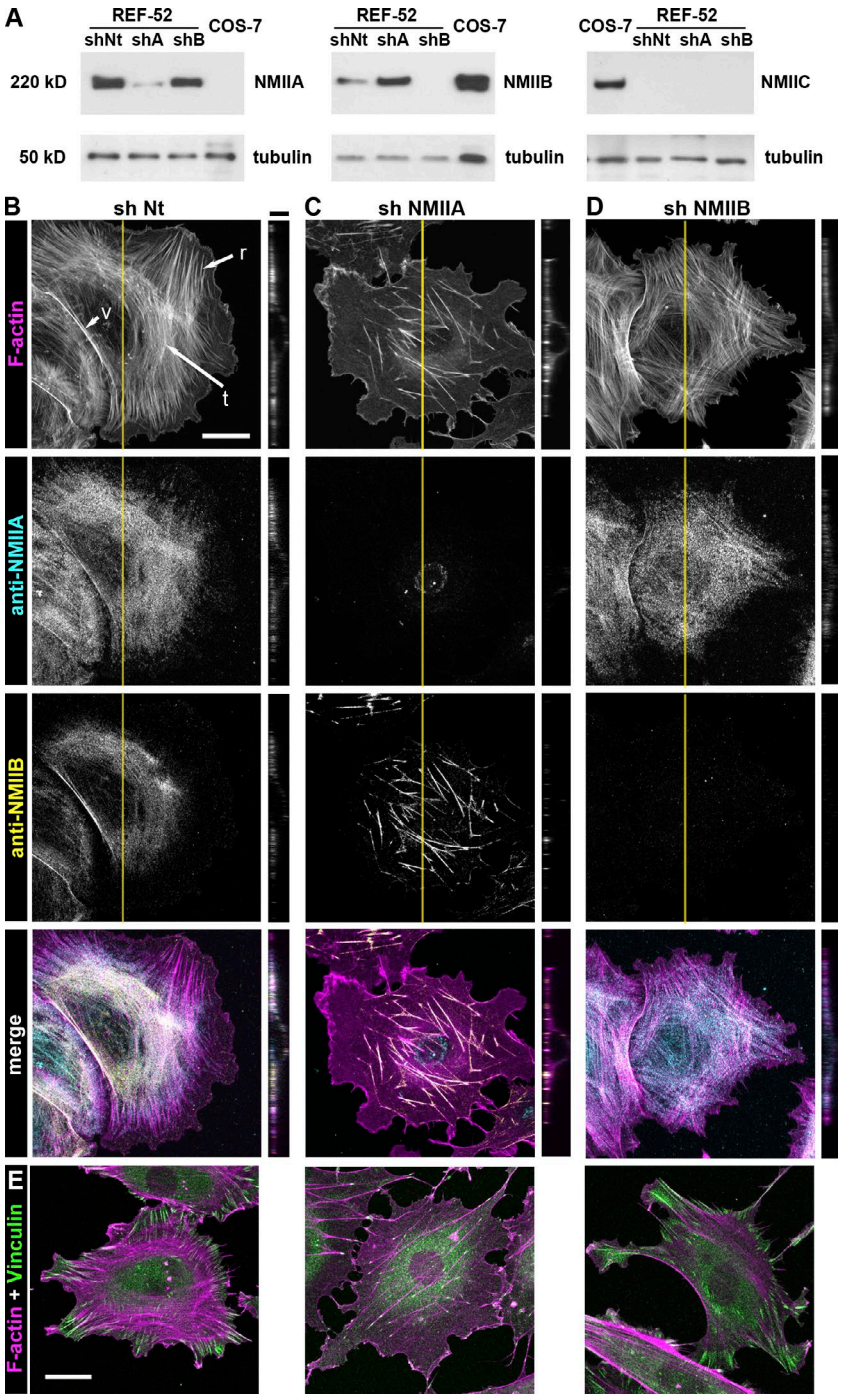

Figure 1. **Organization of stress fibers and distribution of NMIIA and NMIIB in spreading REF-52 fibroblasts with and without depletion of each NMII paralog.** (A) Western blotting showing expression of NMIIA (left), NMIIB (middle), and NMIIC (right) in wild-type COS-7 cells and in REF-52 cells expressing nontargeting shRNA (shNt) or shRNAs targeting NMIIA (shA) or NMIIB (shB). (B–D) REF-52 cells expressing nontargeting shRNA (B, shNt) or shRNA targeting NMIIA (C, sh NMIIA) or NMIIB (D, sh NMIIB). Cells were preextracted before fixation and stained with phalloidin (magenta) and NMIIA (cyan) and NMIIB (yellow) antibodies. Examples of stress fiber types are indicated by arrows in B and show radial (r), ventral (v), and transverse arcs (t). Left panels show xy maximum projections, whereas right panels show z slices along yellow lines. Bars: (xy panels) 20 µm; (z panels) 5 µm. (E) REF-52 cells expressing nontargeting shRNA (left) or shRNA targeting NMIIA (middle) or NMIIB (right). Cells were directly fixed and stained with phalloidin (magenta) and vinculin antibody (green). Bar, 20 µm.

To quantitatively assess these various NMIIB patterns, we analyzed histograms of NMIIB immunofluorescence intensity in raw images (Fig. 3 D). The histogram width reflects the intensity range between the dimmest (at the background level) and the brightest (high NMIIB concentration) pixels in the cell. A relatively uniform distribution of NMIIB observed in cells with high NMIIA expression levels produces a narrow histogram, because these images lack bright pixels and the intensity values cluster close to the abundant dim pixels of the background (Fig. 3 D, right). In contrast, in the presence of a small fraction of very bright pixels that correspond to intense NMIIB clustering in ventral stress fibers, as observed in cells with low levels of NMIIA, the histogram becomes wider because of an extended "tail" of a few bright pixels (Fig. 3 D, left). Plotting the width of the histogram (1–99% of data) against the total fluorescence intensity of GFP-NMIIA in the same cell revealed an inverse relationship between the GFP-NMIIA expression level and the width of the histogram (Fig. 3 E) consistent with the visual impression that increasing levels of NMIIA expression correlated with the progressive dispersion of NMIIB.

These results suggest that the intrinsic propensity of NMIIB to form discrete ventral stress fibers is progressively diminished by the presence of increasing amounts of NMIIA in the cell, suggesting that NMIIA and NMIIB cooperate for stress fiber formation rather than independently drive formation of their preferred stress fiber types.

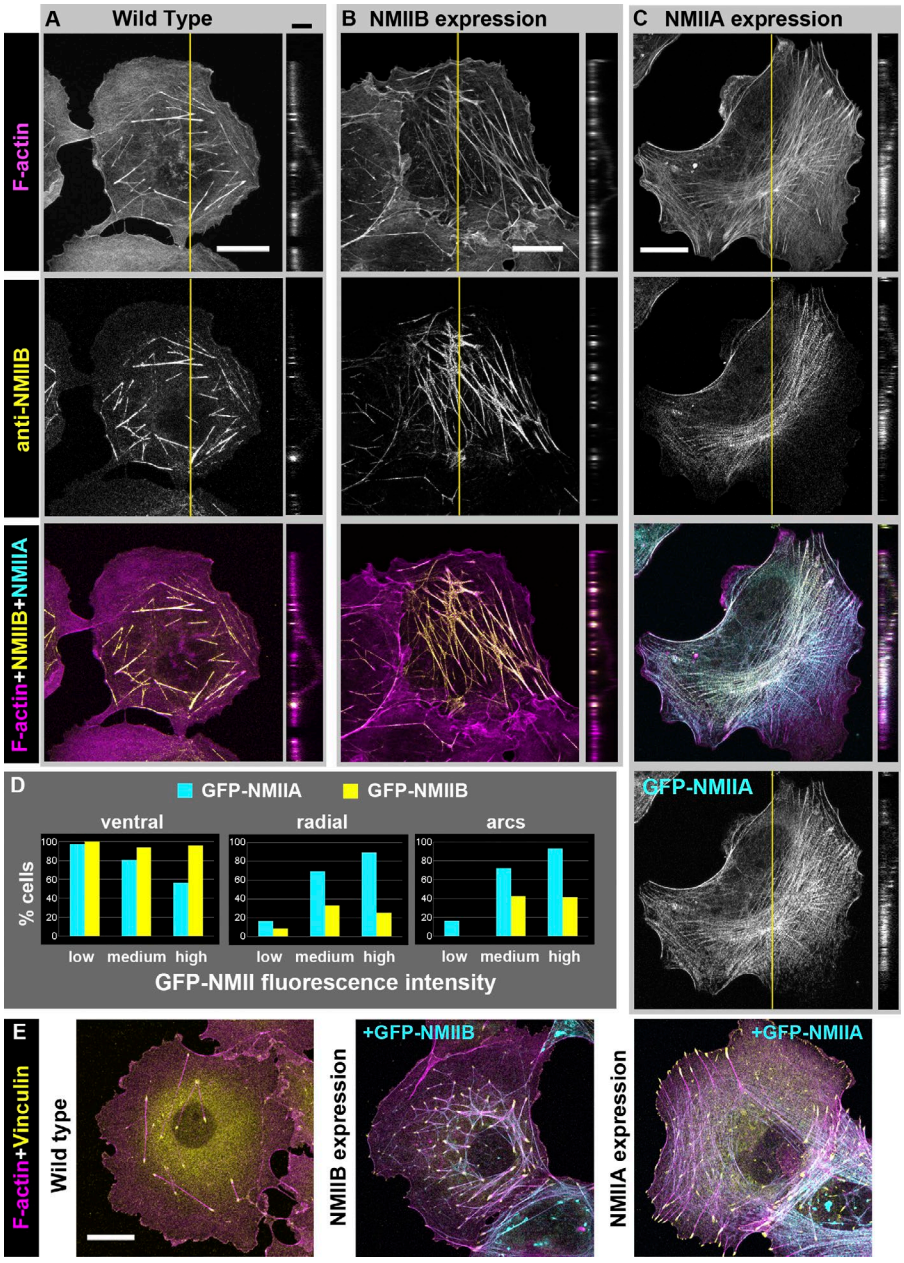

Figure 2. **Organization of stress fibers and distribution of NMIIA and NMIIB in COS-7 cells after ectopic expression of NMIIB or NMIIA.** (A–C) Wild-type cells (A) or cells expressing GFP-NMIIB (B) or GFP-NMIIA (C) fixed and stained with phalloidin (magenta) and NMIIA (cyan) or NMIIB (yellow) antibody. Left panels show xy maximum projections, whereas right panels show z slices along yellow lines. Bars: (xy panels) 20 µm; (z panels) 5 µm. (D) Percentage of cells containing indicated types of stress fibers in groups of cells expressing low, medium, and high levels of GFP-NMIIA (n = 119 cells) or GFP-NMIIB (n = 93 cells). (E) Wild-type cells (left) or cells expressing GFP-NMIIB (middle) or GFP-NMIIA (right) fixed and stained with phalloidin (magenta) and vinculin (green). Bar, 20 µm.

NMIIB becomes more dynamic in the presence of NMIIA

NMIIA is known to be more dynamic than NMIIB both in vitro (Kovács et al., 2007; Nagy et al., 2013; Heissler and Sellers, 2016) and in cells (Sandquist and Means, 2008; Vicente-Manzanares et al., 2008; Raab et al., 2012). However, it is not known whether NMIIA and NMIIB can influence each other's dynamics. Because of dramatic redistribution of NMIIB in the presence of NMIIA, we characterized the dynamics of GFP-NMIIB by FRAP in stress fibers of COS-7 cells expressing GFP-NMIIB alone or GFP-NMIIB together with mCherry-NMIIA (Fig. 4). Analysis of FRAP curves taken from ventral stress fibers revealed a significantly shorter halftime of GFP-NMIIB recovery in cells coexpressing GFP-NMIIB and mCherry-NMIIA (2.3 ± 0.8 min; mean ± SD, n = 7) than in cells expressing GFP-NMIIB alone (8.1 ± 2.4 min; n = 8, $P < 0.01$). The immobile fraction of GFP-NMIIB in ventral stress fibers in the presence and absence of NMIIA remained roughly the same (57 ± 16% and 56 ± 10%, respectively; $P > 0.05$; Fig. 4 F). In transverse arcs of NMIIA-expressing cells (Fig. 4 C), GFP-NMIIB also exhibited fast turnover with the recovery halftime (2.4 ± 0.9 min; n = 6) similar to that observed for NMIIB in NMIIA-positive ventral stress fibers, but with a smaller immobile fraction (31 ± 18%, $n = 6$, $P < 0.05$, Turkey-Kramer multiple comparison test). These data suggest that NMIIA enhances dynamics of NMIIB.

Relative abundance of NMIIA and NMIIB in stress fibers shifts toward NMIIB over time

The accelerating effect of NMIIA on the NMIIB dynamics (Fig. 4) provides a plausible explanation for the observed changes in the NMIIB distribution induced by increasing levels of NMIIA expression (Fig. 3). Specifically, when NMIIA is in a great excess over NMIIB, the dramatically increased NMIIB dynamics would allow NMIIB to be efficiently recycled to the cell periphery leading to broad distribution of NMIIB (Fig. 3 C).

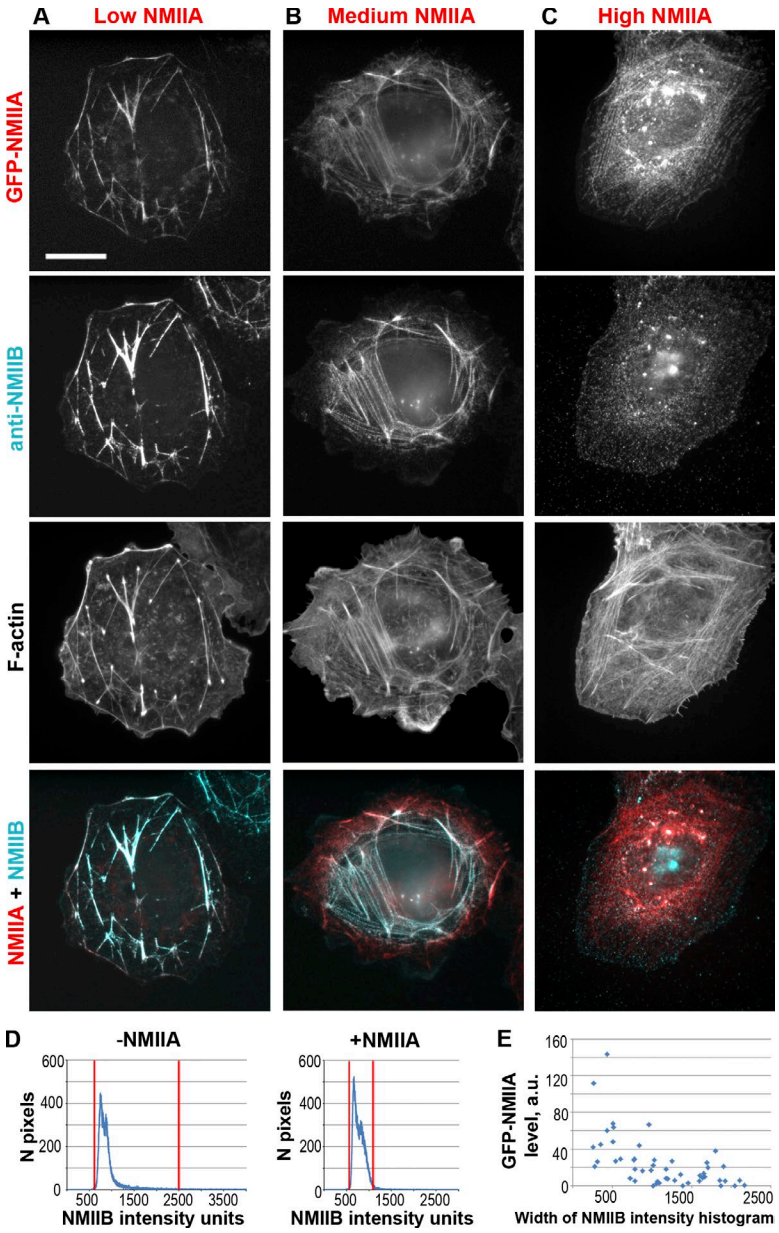

Figure 3. **Redistribution of endogenous NMIIB in COS-7 cells expressing different levels of GFP-NMIIA.** (A–C) Cells with low (A), medium (B), and high (C) expression of GFP-NMIIA (red) fixed and stained with phalloidin and NMIIB antibody (cyan). Bar, 20 µm. (D) Two examples of NMIIB intensity histograms obtained from raw 16-bit images of cells with (right) or without (left) GFP-NMIIA expression. Red lines indicating 1st to 99th percentiles mark the histogram width. (E) Correlation between GFP-NMIIA expression levels (y axis) and the width (1st–99th percentile) of the NMIIB immunofluorescence intensity histogram (x axis; n = 50 cells).

In contrast, low expression levels of NMIIA are not expected to affect the intrinsic accumulation of NMIIB in ventral stress fibers (Fig. 3 A). However, formation of the anterior–posterior NMIIA/NMIIB gradient in cells expressing intermediate levels of NMIIA remains unexplained.

To address this problem, we imaged long-term NMII dynamics in COS-7 cells expressing both mCherry-NMIIA and GFP-NMIIB and exhibiting the NMIIA/NMIIB gradient (Fig. 5 A and Video 1). Stress fibers were constantly formed in the distal lamella (17.4 ± 5.1 stress fibers per 10 h; mean ± SD; n = 9 kymographs from three cells), moved retrogradely and eventually disappeared with a mean lifetime of 154.5 ± 80.5 min (mean ± SD; n = 106 stress fibers from three cells). Importantly, the relative abundance of NMIIA and NMIIB in individual stress fibers showed stereotypical dynamics, in which newly formed stress fibers were enriched in NMIIA relative to NMIIB, whereas over time, NMIIB gradually became the predominant paralog in the same stress fibers. This behavior is best seen in kymographs taken from two-color videos (Fig. 5 A, right). The diagonal streaks in kymographs, which reflect the retrograde flow of individual stress fibers, gradually change their color from red (NMIIA) to white (NMIIA plus NMIIB) to cyan (NMIIB). Notably, the rate of stress fiber retrograde flow either is not changed or decreased when stress fibers become enriched with NMIIB, arguing against a possibility that the front–rear NMIIA/NMIIB gradient results from faster retrograde flow of NMIIB-containing structures. Together, these data suggest that the NMIIA/NMIIB gradient distribution results from gradual replacement of NMIIA by NMIIB in individual stress fibers in parallel with their retrograde flow.

In contrast to very dynamic stress fibers containing NMIIA, stress fibers in COS-7 cells expressing only NMIIB were significantly more stable (Fig. 5, B and C; and Video 2). At low levels of GFP-NMIIB expression, cells contained a few discrete GFP-NMIIB–positive ventral stress fibers (Fig. 5 B) similar to the distribution of endogenous NMIIB in nontransfected cells. Over a period of 10 h, many stress fibers remained largely unchanged (Fig. 5 B and Fig. 5 C, box 3), some underwent

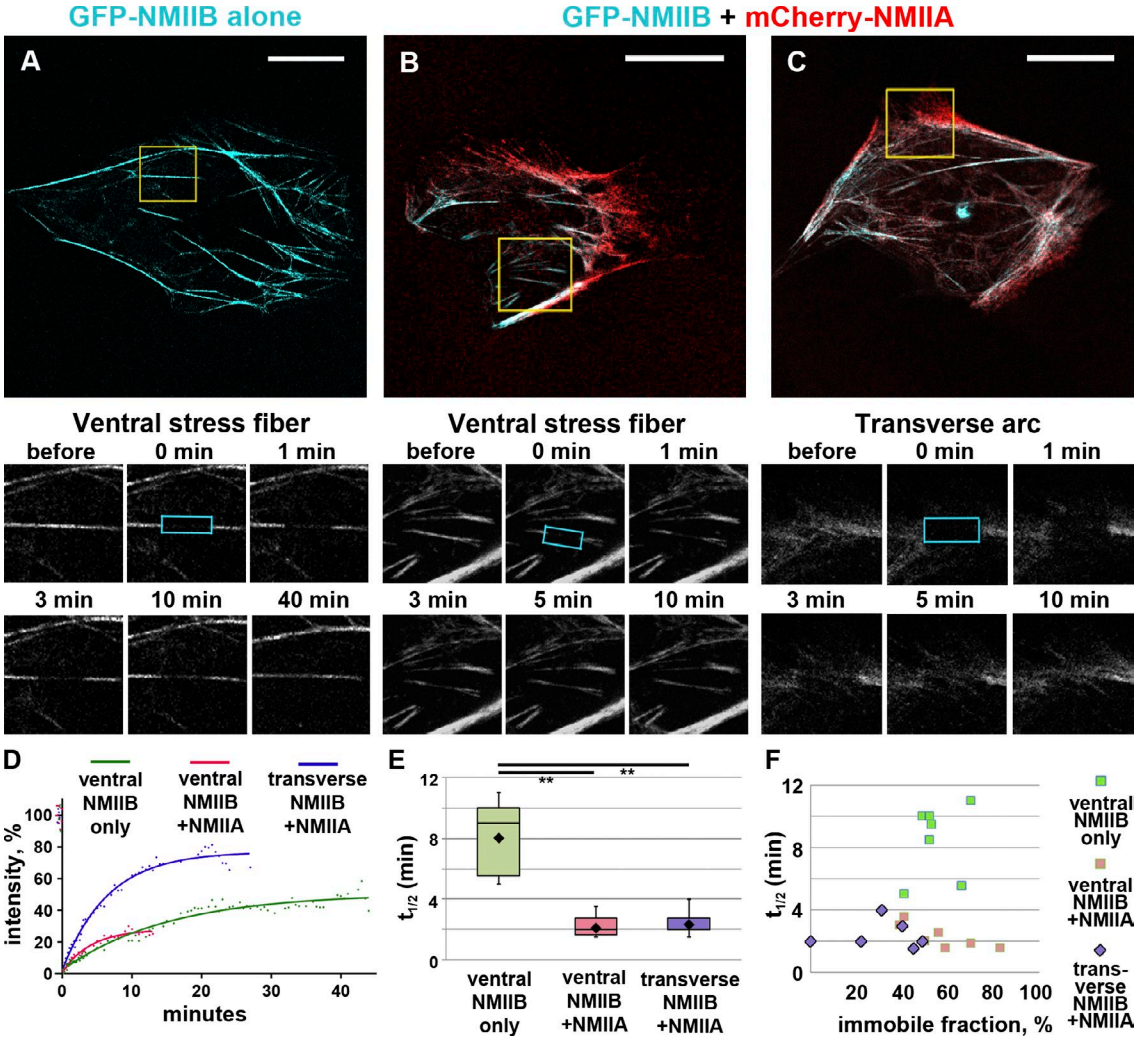

Figure 4. **FRAP analysis of GFP-NMIIB in COS-7 cells in the presence or absence of NMIIA.** (A–C) Examples of cells expressing GFP-NMIIB alone (A) or GFP-NMIIB together with mCherry-NMIIA (B and C). (Top) Prebleach image of the cell showing GFP-NMIIB (cyan) and mCherry-NMIIA (red). (Bottom) Time frames of the boxed region (15 × 15 µm) before or at indicated times after photobleaching of a ventral stress fiber (A and B) or a transverse arc (C). Bleached regions are marked by a blue box. Bars, 20 µm. (D) FRAP curves corresponding to regions shown in A–C. (E) Halftimes of GFP-NMIIB recovery for indicated conditions. Top and bottom of a box indicate 75th and 25th quartiles, respectively; whiskers encompass all data, the dot is the mean, and and the middle line is the median. Asterisks indicate statistical significance (**, $P < 0.01$, Dunn's multiple comparisons test). (F) Individual FRAP data points.

contraction (Fig. 5 C, box 4), and only a few new stress fibers were formed (1.7 ± 1.5 stress fibers per 10 h; mean ± SD; $n = 18$ kymographs from seven cells). De novo stress fiber formation occurred by slow coalescence of smaller and fainter tangential bundles (Fig. 5 C, boxes 1 and 2), qualitatively resembling the process described for other stress fibers (Hotulainen and Lappalainen, 2006). These results suggest that when stress fibers containing both NMIIA and NMIIB become enriched with NMIIB, they become much more stable.

NMIIA facilitates directional cell migration, whereas excess of NMIIB suppresses migration

Our data indicate that organization of the actin cytoskeleton in cells depends on cooperation of NMIIA and NMIIB. We next investigated whether changes in the NMIIA and/or NMIIB expression levels alter cell migration.

We first analyzed random cell motility by tracking nuclei of individual cells for 16 h (Fig. 6 A). In REF-52 cells, knockdown of NMIIA slightly, but significantly decreased the speed of cell migration compared with cells treated with nontargeting shRNA. In contrast, depletion of NMIIB had no effect on the speed of REF-52 cells. To determine whether slower cell migration of NMIIA-knockdown cells was caused by a reduction in the total levels of NMII or was specific to NMIIA depletion, we overexpressed GFP-NMIIB in NMIIA-depleted REF-52 cells. However, instead of rescuing cell migration, overexpression of GFP-NMIIB further decreased the speed of the NMIIA-knockdown cells (Fig. 6 A). Similar trends could be detected in COS-7 cells. Wild-type COS-7 cells moved very slowly. Overexpression of GFP-NMIIA or GFP-NMIIB resulted in an apparent increase and decrease of the cell speed, respectively, although these differences did not reach statistical significance compared with wild-type cells. However, COS-7 cells overexpressing NMIIA moved significantly faster than cells overexpressing NMIIB. These data suggest that NMIIA has migration-promoting effects, at least in certain conditions, whereas excessive NMIIB may slow down cell migration.

In line with this suggestion, NMIIA but not NMIIB has been recently shown to be required for the chemotaxis of mouse

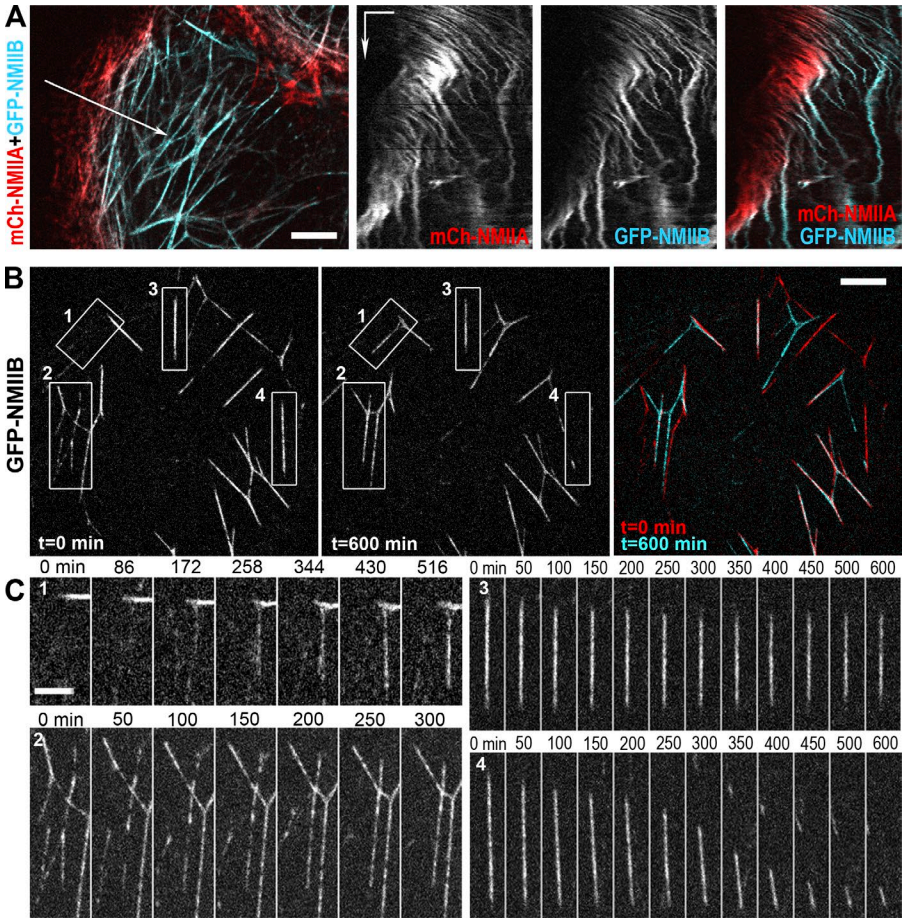

Figure 5. **Long-term dynamics of stress fibers in COS-7 cells expressing NMIIB only or NMIIA and NMIIB together.** (A) COS-7 cells expressing GFP-NMIIB (cyan) and mCherry-NMIIA (red). (Left) First frame of the video. (Right) Kymographs along the arrow in the left panel showing two channels separately and as a merged image. Bar, 10 µm. Kymograph showing the distance bar (horizontal), 5 µm, and time bar (vertical), 2 h. (B and C) COS-7 cell expressing GFP-NMIIB only shows very slow stress fiber dynamics. (B) First (left) and last (middle) frames of the time-lapse sequence are overlaid at right. Stress fibers that appear white are largely unchanged after 10 h. Bar, 10 µm. (C) Time frames showing dynamics of individual stress fibers marked by numbered boxes in B. (1 and 2) Assembly of new stress fibers from faint tangential arcs. (3) Stable stress fiber. (4) Contracting stress fiber. Bar, 5 µm.

embryo fibroblasts (Asokan et al., 2014). We reasoned that differences in directional cell migration of REF-52 and COS-7 cells expressing different NMII paralogs could be more apparent during chemotaxis. Therefore, we performed a microfluidic chemotaxis assay where cells moved up a PDGF gradient (Wu et al., 2012). We found that cells containing NMIIA, such as control and NMIIB-depleted REF-52 cells and COS-7 cells ectopically expressing NMIIA, were able to move directionally up the gradient. In contrast, NMIIA-knockdown REF-52 cells and wild-type COS-7 cells, which did not express NMIIA, could not chemotax, and overexpression of GFP-NMIIB was not able to rescue chemotaxis in these cells (Fig. 6, B and C).

NMIIA is mainly responsible for cell contractility

Different motor properties of NMIIA and NMIIB make them more suitable for generating contraction and holding tension, respectively (Kovács et al., 2007; Billington et al., 2013; Nagy et al., 2013; Heissler and Sellers, 2016). To compare contractile properties of REF-52 cells that express NMIIA and NMIIB either individually or together, we used traction force microscopy (Fig. 6, D and E). REF-52 cells expressing nontargeting shRNA generated significant traction forces on fibronectin-coated hydrogels with 25 kPa stiffness. Depletion of NMIIB had no measurable effect on cell contractility. In contrast, knockdown of NMIIA significantly decreased traction forces to very low levels. These results are consistent with previous findings in other cells types (Cai et al., 2006; Jorrisch et al., 2013; Thomas et al., 2015). However, these results can potentially be explained by reduction of the total NMII level after knockdown of abundant NMIIA. To compensate for total NMII loss, we overexpressed NMIIB in NMIIA-depleted cells. However, overexpressed NMIIB did not rescue the loss of contractility in NMIIA-depleted cells. These data suggest that NMIIA is primarily responsible for cell contraction, whereas NMIIB may play a role in stabilizing the cytoskeleton.

Discussion

Collectively, our results show that although NMIIA and NMIIB intrinsically favor formation of distinct stress fiber types, they also cooperate with each other in cells. Evidence for cooperation comes from the ability of NMIIA to induce redistribution of NMIIB and enhance its dynamics in cells. At a certain expression ratio, NMIIA and NMIIB develop a polarized distribution in the cell using a self-sorting process, in which a gradual increase of the NMIIB/NMIIA ratio in stress fibers occurs in parallel with their retrograde flow. On the functional side, NMIIA promotes cell migration, chemotaxis, and traction force generation, whereas excessive NMIIB may interfere with these processes. These distinct functions of NMIIA and NMIIB together with their ability to cooperate and segregate in the cell suggest that various cell types can differently organize their actin cytoskeleton by regulating relative expression levels of NMIIA and NMIIB, whereas particular cytoskeleton organization would allow the cell to perform specialized functions.

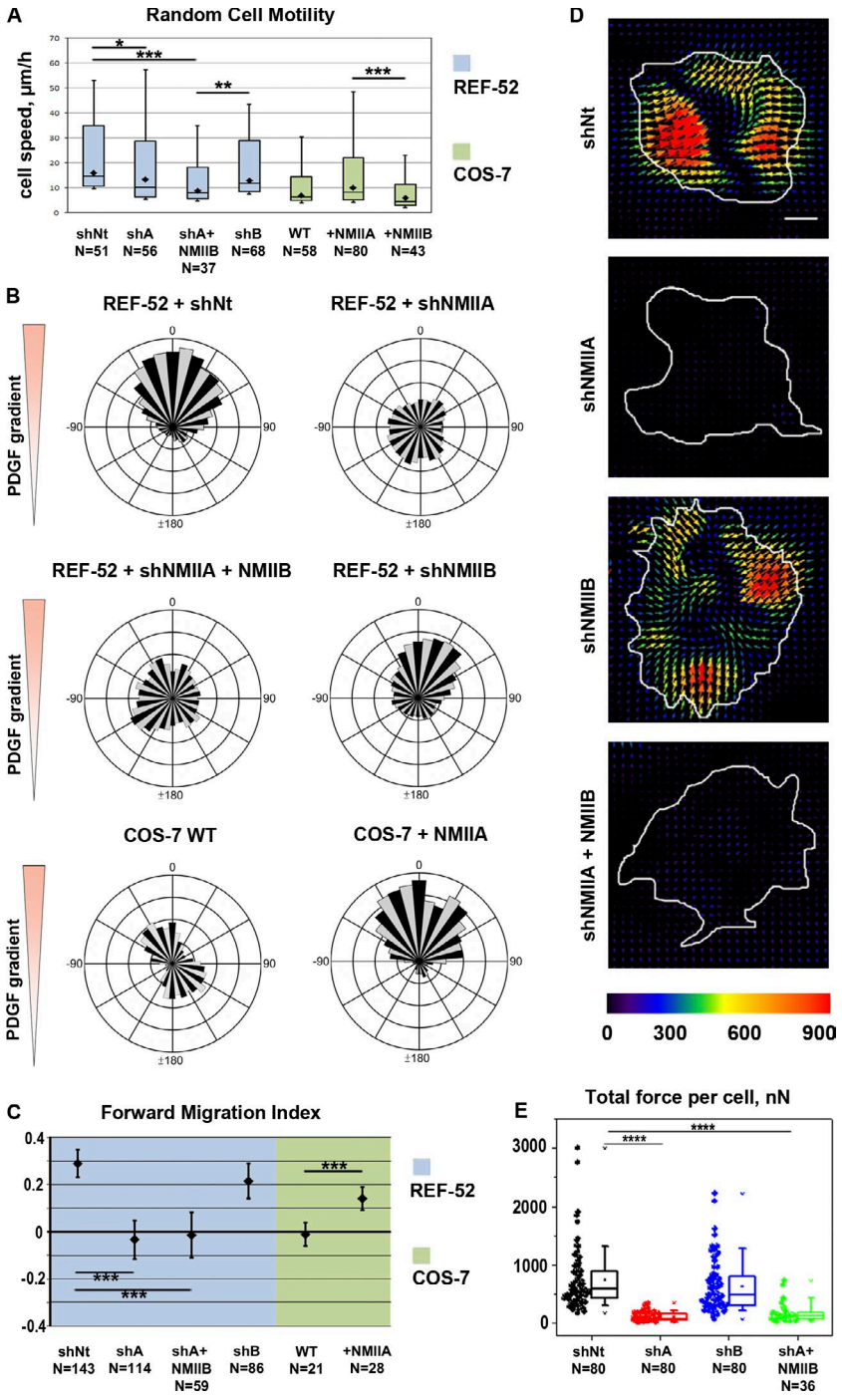

Figure 6. **Migration, chemotaxis, and traction forces of cells with different expression patterns of NMIIA and NMIIB.** (A) Speed of randomly migrating REF-52 and COS-7 cells in indicated conditions. Top and bottom of a box indicate 75th and 25th quartiles, respectively; whiskers encompass all data, the dot is the mean, and the middle line is the median. Asterisks indicate statistical significance (*, $P < 0.05$; **, $P < 0.01$; ***, $P < 0.001$, Dunn's multiple comparisons test); N, number of cells. (B) Wind-rose histograms of PDGF chemotaxis of REF-52 and COS-7 cells expressing indicated constructs. The length of each leaflet corresponds to the percentage of cells migrating in the direction of leaflet. (C) Forward migration indices of REF-52 and COS-7 cells migrating toward the PDGF gradient (mean ± 95% confidence interval). Forward migration index reflects directionality; values >0.1 are considered directional. Asterisks indicate statistical significance (***, $P < 0.001$, Dunn's multiple comparisons test); N, number of cells. (D) Examples of traction stress maps for REF-52 cells on ∼25-kPa polyacrylamide gels in indicated conditions. Bar, 20 µm; color bar units, pascals. (E) Plot with quantification of total force per cell (****, $P < 0.0001$, nonparametric ANOVA with Dunn's multiple comparisons test).

A mechanistic explanation for the preferential assembly of NMII-specific stress fiber types is relatively straightforward, because behavior of these stress fibers matches the known kinetic properties of respective NMII paralogs. The NMIIB motor has a high duty ratio that is further increased under resistive load (Kovács et al., 2007; Nagy et al., 2013; Heissler and Sellers, 2016). Also, NMIIB filaments undergo slower turnover in cells compared with NMIIA (Sandquist and Means, 2008; Vicente-Manzanares et al., 2008; Raab et al., 2012). These features make NMIIB less efficient in rearranging actin structures but more capable of cross-linking actin filaments into stable bundles. Accordingly, NMIIB in the absence of NMIIA supports formation of stable and strongly attached but poorly contractile ventral stress fibers. They can retard cell migration in both random migration and chemotaxis assays, especially after NMIIB overexpression. In contrast, the NMIIA motor has a short duty ratio with low load dependence and fast ATPase activity (Billington et al., 2013), whereas NMIIA filaments exhibit rapid turnover in cells (Sandquist and Means, 2008; Vicente-Manzanares et al., 2008; Raab et al., 2012). Accordingly, NMIIA in the absence of NMIIB promotes formation of a highly dynamic system of radial stress fibers and transverse arcs. This system exerts significant traction forces and is capable of fast reorganization during cell migration, especially in response to external cues (Asokan et al., 2014; this study).

A much less predictable discovery in our study is the ability of NMIIA to "dynamize" NMIIB and to regulate the NMIIB distribution in the cell. These findings suggest that NMIIB and NMIIA cooperate with each other. If two paralogs behaved independently, they would segregate into NMIIB-dependent ventral stress fibers and NMIIA-dependent transverse arcs even when present together in the same cell. Although the idea of cooperation of different NMII paralogs is rather intuitive, especially after discovery of copolymerization of NMII paralogs (Beach et al., 2014; Shutova et al., 2014), the supporting experimental evidence was not previously available and the underlying mechanism was not defined.

We propose that cooperation of NMII paralogs occurs through their copolymerization. Our mechanistic model is based on two key assumptions: (1) polymerization-competent NMIIA and NMIIB monomers assemble into filaments with equal probability and proportionally to their availability, and (2) NMIIA and NMIIB subunits dissociate from NMII filaments with different paralog-specific rates (Fig. 7). These assumptions are based on the existing knowledge about mechanisms of NMII assembly and disassembly. To enable NMII polymerization, NMII molecules are first activated by phosphorylation of the regulatory light chain, which is shared by NMII paralogs. Subsequently, NMII polymerization is governed by two assembly competence domains in the NMII heavy chain (Nakasawa et al., 2005; Ricketson et al., 2010), which are virtually identical for NMIIA and NMIIB. Therefore, both paralogs are expected to polymerize with the same efficiency into homo- and heteropolymers, as we indeed have observed (Shutova et al., 2014). On the other hand, subunit dissociation from NMII filaments is thought to depend on the C-terminal region of the NMII heavy chains, which is targeted by kinases and interaction partners that can promote filament disassembly (Dulyaninova and Bresnick, 2013). This region is highly divergent among NMII paralogs, suggesting that subunit dissociation is controlled by different mechanisms for different paralogs. Accordingly, available data suggest that NMIIA has a faster turnover than NMIIB (Sandquist and Means, 2008; Vicente-Manzanares et al., 2008; Raab et al., 2012).

Based on these two postulates, we can accurately explain our experimental results. When both NMIIA and NMIIB are present in the cells, at a low NMIIA/NMIIB ratio, NMII filaments are dominated by NMIIB subunits. They are expected to behave similar to pure NMIIB filaments, because a low fraction of NMIIA subunits can neither overcome the force-holding behavior of many NMIIB subunits nor increase the filament turnover rate. Even if NMIIA subunits dissociate at their intrinsic fast rate, the majority of slow-cycling NMIIB subunits can maintain the filament integrity, and the cell will form mostly stable ventral stress fibers, similar to cells having only NMIIB. In contrast, at a high NMIIA/NMIIB ratio, too few NMIIB subunits in the NMIIA-dominated filaments are insufficient to restrain the fast motor activity of the NMIIA majority. Furthermore, when NMIIA subunits dissociate at their characteristic fast rate, the few remaining NMIIB subunits cannot stay in a filamentous form and are forced to recycle as well. Consequently, cells will form a dynamic stress fiber system typical for NMIIA alone, whereas NMIIB will behave similar to NMIIA. These considerations explain the faster turnover rate of NMIIB and its broader distribution in the presence of abundant NMIIA.

When NMIIA and NMIIB are present at competitive levels, the heterotypic filaments will exhibit new characteristics.

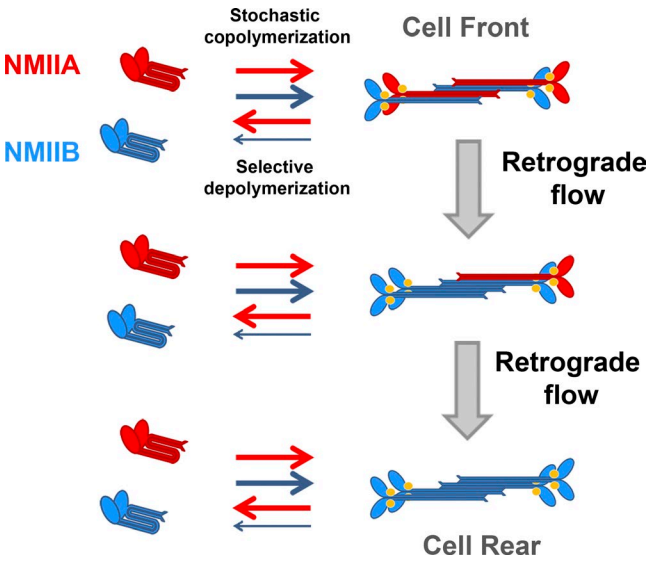

Figure 7. **Model of indiscriminate copolymerization and selective depolymerization of NMIIA and NMIIB explaining self-organization of NMII paralogs into a polarized contractile system in motile cells.** Polymerization of NMIIA (red) and NMIIB (blue) monomers occurs with similar efficiency (forward arrows), whereas their dissociation rates (reverse arrows) are different. Faster dissociation of NMIIA subunits together with equivalent addition of new NMIIA and NMIIB subunits leads to gradual accumulation of NMIIB in old filaments during their centripetal drift because of retrograde actin flow.

Even when the fast-cycling NMIIA subunits dissociate from such filaments, a sufficient number of remaining NMIIB subunits can prevent the filament from falling apart. New NMIIA and NMIIB subunits will be then added to NMIIB-enriched filaments in proportion to their abundance in the monomer pool. Repeating cycles of indiscriminate recruitment of new subunits and preferential dissociation of NMIIA subunits will gradually increase the fraction of NMIIB subunits in heterotypic NMII filaments. This mechanism explains the gradual increase of the NMIIB/NMIIA ratio in stress fibers with time. Because the entire actin–NMII array undergoes retrograde flow, older filaments enriched with NMIIB subunits will be gradually shifted away from the leading edge, where the younger NMIIA-enriched filaments are formed. This process will create the anterior–posterior NMIIA/NMIIB gradient.

The gradient distribution of NMIIA and NMIIB along the front–rear axis is well known (Maupin et al., 1994; Kelley et al., 1996; Kolega, 1998; Saitoh et al., 2001; Vicente-Manzanares et al., 2008) and thought to contribute to maintenance of cell polarity (Vicente-Manzanares et al., 2011). However, the mechanism of the spatial segregation of NMIIA and NMIIB was unclear. It was proposed to depend on delayed incorporation of NMIIB filaments into preformed actin–NMII bundles seeded by NMIIA (Vicente-Manzanares et al., 2008) or paralog-specific targeting of NMII molecules to respective cell regions (Sandquist and Means, 2008; Juanes-Garcia et al., 2015). However, we have recently shown that NMIIA and NMIIB simultaneously incorporate into newly formed structures, whereas their segregation occurs much later (Shutova et al., 2014). These data, as well as our current finding that the NMIIA/NMIIB gradient is formed only at an optimal NMIIA/NMIIB ratio, are incompatible with these previous models. Interestingly, analysis of NMIIA/NMIIB chimeras demonstrated that relative

distribution of these mutants along the anterior–posterior axis is governed by the C-terminal tails of NMII heavy chains (Sandquist and Means, 2008). Although this finding was interpreted as tail-dependent targeting of NMII paralogs, it is fully consistent with our model, because the formation of the NMIIA/NMIIB gradient in our model depends on differential NMII turnover, which is controlled by the heavy chain tails.

Cooperativity between NMII paralogs can help explain some discrepancies regarding roles of NMIIA and NMIIB in cell migration. For example, both decreased (Betapudi et al., 2006; Kim and Adelstein, 2011) and increased (Sandquist et al., 2006; Even-Ram et al., 2007; Shih and Yamada, 2010; Doyle et al., 2012; Jorrisch et al., 2013) rates of cell migration were reported after interfering with NMIIA functions. As a fast motor mainly responsible for cell contractility, NMIIA can stimulate cell migration by retracting the cell rear and providing traction at the cell front, but it also can inhibit migration by counteracting the leading edge protrusion. What activity of NMIIA prevails may depend on the presence and abundance of NMIIB. Different phenotypes also have been reported to result from NMIIB deficiency. In our experiments and some other studies (Shih and Yamada, 2010; Doyle et al., 2012; Jorrisch et al., 2013), NMIIB deficiency did not lead to defects in cell migration and chemotaxis, but it resulted in slower (Betapudi et al., 2006; Sandquist et al., 2006; Kim and Adelstein, 2011; Thomas et al., 2015) or faster (Lo et al., 2004) cell migration in other cases. The ability of NMIIB to stabilize a polarized cell shape (Vicente-Manzanares et al., 2008) can explain decreased cell migration after NMIIB depletion. However, our results showing that NMIIB-positive cells lacking NMIIA are poorly polarized suggest that stabilization of cell polarity is not a role of NMIIB per se (Vicente-Manzanares et al., 2011) but rather requires an optimal ratio of NMIIB/NMIIA and their cooperation. Nevertheless, in the presence of other polarizing cues, such as a chemotactic gradient, the role of NMIIB in polarization may be dispensable, as observed in our experiments. In cases when cells have large excess of NMIIA over NMIIB, the contribution of NMIIB to cell migration may be rather subtle and detectable only in some special conditions. On the other hand, if cells have a high NMIIB/NMIIA ratio, then NMIIB down-regulation may increase the cell migration speed (Lo et al., 2004). In this study, we did not investigate a role of NMIIC in the cytoskeletal organization and cell migration. However, because organization of stress fibers in wild-type COS7 cells containing both NMIIB and NMIIC is very similar to that of NMIIA-knockdown REF52 cells containing only NMIIB, NMIIC may not play a significant role in the processes studied here. Roles of NMIIC in cell physiology could be a subject of future research.

In conclusion, our study shows that NMIIA and NMIIB cooperate in cells through copolymerization. Notably, our data also reveal physiological significance of copolymerization of NMII paralogs (Beach et al., 2014; Shutova et al., 2014) that so far remained obscure (Beach and Hammer, 2015). Depending on the relative abundance of NMIIA and NMIIB, cells can form bipolar filaments with a whole range of dynamic properties. These diverse filaments can favor formation of different stress fiber arrays, which are suitable for specific functions in different cell types. Therefore, the ability of NMII to polymerize into bipolar filaments is necessary for not only generating contraction but also fine-tuning NMII's roles as a motor, cross-linker, and organizer of actin networks.

Materials and methods

Cell culture

REF-52 rat embryo fibroblasts (Verkhovsky et al., 1995) and COS-7 green monkey kidney cells (Applewhite et al., 2007) were cultured in DMEM (Gibco) supplemented with 10% FBS (Gibco) and penicillin/streptomycin at 37°C and 5% CO_2. For experiments, cells were plated on glass coverslips and allowed to spread for 3 h (REF-52) or overnight (COS-7). For live-cell imaging, cells were plated on glass-bottom 35-mm Petri dishes (MatTek Corporation) in CO_2-independent L15 medium supplemented with 10% FBS.

Plasmids, shRNA construction, and transfection

pCMV-mCherry-MHC-IIA was a gift from V. Betapudi (Case Western Reserve University, Cleveland, OH; plasmid 35687; Addgene; Dulyaninova et al., 2007); CMV-GFP-NMHC II-A and CMV-GFP-NMHC II-B were a gift from R. Adelstein (National Heart, Lung, and Blood Institute, Bethesda, MD; plasmids 11347 and 11348; Addgene; Wei and Adelstein, 2000). Cells were transfected using the Neon Transfection System (Thermo Fisher Scientific) according to the manufacturer's online protocols for COS-7 and mouse embryo fibroblasts. For chemotaxis assay, COS-7 cells were transfected using with Lipofectamine 2000. The cells were analyzed 1 or 2 d after transfection.

For the shRNA design, the following targeting sequences were used: 5′-GATCTGAACTCCTTCGAGC-3′ (to target rat NMIIA) and 5′-GGATCGCTACTATTCAGGA-3′ (to target rat NMIIB; Vicente-Manzanares et al., 2007). The sequence 5′-GCCATTCTATCCTCT AGAG-3′ was used as a nontargeting control. Oligos for shRNA construction were obtained from Integrated DNA Technologies and cloned into HpaI and XhoI restriction sites of the lentiviral PLL-GFP 5.0 and PLL-Cerulean 5.0 vectors (gift from A. Efimov, Fox Chase Cancer Center, Philadelphia PA; Smalley-Freed et al., 2010). For producing lentiviral particles, plasmids containing shRNA sequences were cotransfected together with helper plasmids MD2G and Pax2 into HEK-293T cells using FuGENE-6 (Roche). The virus was harvested on the third day after transfection and immediately applied to cell cultures with addition of 5 µg/ml protamine sulfate (Sigma). Culture medium was replaced after 6 h incubation with the virus, and cells were cultured for additional 6 d or more before analysis.

Western blotting

Cells were washed in ice-cold PBS and lysed in ice-cold lysis buffer (20 mM Tris, 500 mM NaCl, 1 mM EDTA, and 0.5% Triton, pH 7.5) containing Phosphatase Inhibitor Cocktail 2 and Protease Inhibitor Cocktail (Sigma). After centrifugation at 13,000 *g* for 10 min at 4°C, supernatants were mixed with the NuPAGE sample buffer (Invitrogen) supplemented with 200 mM DTT and heated at 75°C for 5 min. Approximately 2.5 to 5 µg total protein was loaded onto 3–8% NuPAGE TA 1.0 gradient gels (Invitrogen), resolved by SDS-PAGE, and transferred to a 0.45-µm polyvinylidene fluoride membrane in NuPAGE Transfer Buffer at 20 V for 2 h using the X Cell SureLock Electrophoresis and Western Blotting System (Invitrogen). The membrane was blocked for 1 h with 5% dry milk in TBS (Bio-Rad) containing 0.1% Tween-20 (Sigma), incubated with primary antibodies in TBS/Tween-20 for 2 h, washed in TBS/Tween-20, incubated with secondary antibodies for 1 h, and developed with Enhanced Chemiluminescence Western Blotting Detection Reagent (GE Healthcare). The following antibodies were used: mouse monoclonal antibody to NMIIA (ab55456; 1:30,000; Abcam), rabbit polyclonal antibody to NMIIB (3404; 1:1,000; Cell Signaling), mouse monoclonal antibody to α-tubulin (T9026; 1:5,000; Sigma), and horseradish peroxidase–linked enhanced chemiluminescence anti–mouse and anti–rabbit IgG (1:20,000; GE Healthcare).

Fluorescence microscopy, live-cell imaging, and FRAP

For immunofluorescence staining, cells were either directly fixed with 4% formaldehyde in PBS for 10 min, or preextracted with 0.5% Triton X-100 in PEM buffer (100 mM Pipes-KOH, pH 6.9, 1 mM $MgCl_2$, 1 mM EGTA, and 2 µM unlabeled phalloidin). Directly fixed samples were then permeabilized with 0.1% Triton X-100. The following primary antibodies were used: mouse monoclonal antibody to NMIIA (ab55456; Abcam), rabbit polyclonal antibody to NMIIB (3404; Cell Signaling), and mouse monoclonal antibody to vinculin (clone hVIN1; Sigma). Secondary Alexa Fluor 647– and Alexa Fluor 594–labeled anti–mouse and anti–rabbit antibodies were from Molecular Probes. F-actin was stained with Alexa Fluor 488 and 594 phalloidin (Molecular Probes). Coverslips were mounted with Prolong Gold antifade reagent (Invitrogen).

Wide-field fluorescence microscopy of fixed samples was performed using Eclipse TE2000-U inverted microscope (Nikon) equipped with Plan Apo 100× 1.3 NA oil-immersion objective lens and Plan Apo 20× lens and Cascade 512B CCD camera (Photometrics) driven by Metamorph imaging software (Molecular Devices).

Confocal microscopy and FRAP experiments were performed using a TCS SP8 microscope (Leica Microsystem) equipped with 63× 1.4 NA oil-immersion objective, 405-, 488-, 552-, and 638-nm excitation laser lines and photomultiplier tubes and HyD detectors driven by LAS software (Leica Microsystem). Images were collected at pinhole 1.0, with step size 0.3 µm. FRAP experiments were done in one confocal plane, using the following conditions: 10 "pre-bleach" frames acquired at maximum speed (488-nm laser at 2% power); photobleaching of selected regions was done with 488-nm laser at 50% power (maximum speed, five times); "post-bleach" acquisition was done with 488-nm laser at 2% power, with 30 s between frames. Fluorescence intensity of the acquired images was analyzed in Metamorph. Contrast of images was linearly adjusted to optimally reveal features of interest in individual images.

Live-cell imaging of randomly moving cells was performed using Nikon Eclipse Ti inverted microscope equipped with Plain Apo 20× 0.75 objective and QuantEM 512SC digital camera (Photometrics) driven by NIS-Elements software (Nikon). Images were collected every 10 min for up to 16 h. Tracks of individual interphase cells were built and analyzed in ImageJ based on the position of the cell nucleus. Two independent experiments were performed for each condition. Statistical analyses were performed using Excel (Microsoft) or Instat (GraphPad Software) software packages.

Spinning disk confocal imaging of living cells expressing Cherry-NMIIA and/or GFP-NMIIB was performed on an Eclipse Ti inverted microscope equipped with 100× objective and QuantEM 512SC digital camera driven by NIS-Elements software. Single confocal planes were taken every 2 min for 10 h.

Chemotaxis assay

Transfected cells were sorted using a Bio-Rad S3 sorter. Polydimethylsiloxane microfluidic devices were prepared as described previously (Wu et al., 2012). Chemotaxis assays were performed on an IX81 microscope (Olympus) with a 20× objective lens using Metamorph imaging software. Images were collected every 10 min for up to 24 h. Individual cells were manually tracked using ImageJ software (Manual Tracking plugin). Only viable and visibly migrating cells (net path length >50 µm) were tracked. The tracks obtained were analyzed using the Chemotaxis Tool ImageJ plugin (http://www.ibidi.de/applications/ap_chemotaxis.html#imageanalysis). This analysis tool was used to extract the forward migration index, which is a net distance moved in the direction of the gradient divided by total path length. The plugin also generates histograms (count frequency) of migration direction of cells for each dataset. The secplot function of MATLAB was then used to generate rose plots of directional migration on normalized polar coordinates, where the outermost ring corresponds to frequency (r) of 8%.

Traction force microscopy

Polyacrylamide hydrogels (Young's modulus, E = ∼25 kPa) coated with 5 µg/ml fibronectin were prepared as previously described (Cretu et al., 2010). Before polymerization, 0.2-µm-diameter fluorescent microspheres (No. F8810; Invitrogen) were added into polyacrylamide mixture at 1% vol/vol. Hydrogels were subsequently washed three times with PBS and incubated with culture medium for 30 min before plating cells. In all traction force experiments, REF-52 cells stably transfected with GFP- or Cerulean-expressing shRNA constructs were seeded at a density of 3,000 cells/cm^2 and allowed to attach for 4 h before imaging. Fluorescence images of cells and embedded beads were captured at 20× magnification using Olympus IX70 inverted microscope equipped with Photometrics CoolSnap HQ CCD camera and driven by Deltavision Softworx software (GE Healthcare Life Sciences). Image sequences for each chosen field were taken at two points before and after cell lysis with an SDS buffer. All imaging was performed in an environmental chamber (37°C, 5% CO_2). Traction force microscopy data analysis (stack alignment, particle image velocimetry, and Fourier transform traction cytometry) was performed using a freely available plugin suite for ImageJ (created by Tseng et al., 2012; adapted from Dembo and Wang, 1999). For Fourier transform traction cytometry, the Poisson's ratio of the polyacrylamide gel was assumed to be 0.45 and a regularization parameter of 10^{-9} was used. Traction force vector maps were analyzed using a custom MATLAB script to determine mean traction stress generated by each cell and total force exerted per cell. Cell area was determined from the corresponding images of GFP fluorescence in ImageJ.

Image analyses

Quantification of stress fiber types in COS-7 cells. Wide-field images of randomly chosen cells expressing GFP-NMIIA (n = 119 cells) or GFP-NMIIB (n = 93 cells) and stained for F-actin were analyzed. For each cell, the intensity of GFP in 16-bit images was measured after background subtraction using Metamorph. Based on the intensity of GFP, the cells were categorized into three groups based on expression (no/low, medium, and high; roughly the same number of cells was assigned to each group). Stress fiber types were visually determined in phalloidin-stained images after application of Laplase2 filter in Metamorph to sharpen individual stress fibers.

Distribution of NMIIB within the cell. Wide-field 16-bit images of randomly chosen cells from cell culture transfected with GFP-NMIIA and stained with NMIIB antibody and F-actin were analyzed (n = 50 cells). The cell boundary was defined using F-actin images. The integrated intensity of GFP-NMIIA for each cell was measured in Metamorph after background subtraction and was represented in arbitrary units. The histograms of NMIIB staining intensity within the cell boundary were obtained in Metamorph using raw 16-bit images. A histogram represents distribution of pixels according to their intensity; therefore, the histogram width reflects the intensity range between the dimmest and the brightest pixels in the cell. Histogram widths were defined as intensity range between 1% dimmest pixels in the cell and 1% brightest pixels in that cell (1–99%).

Online supplemental material

Video 1 shows the long-term dynamics of stress fibers in COS-7 cells expressing GFP-NMIIB and mCherry-NMIIA. Video 2 shows the long-term dynamics of stress fibers in COS-7 cells expressing low levels of GFP-NMIIB.

Acknowledgments

We thank Dr. Andrea Stout and the Cell and Developmental Biology Microscopy Core at the University of Pennsylvania for help with FRAP experiments and Dr. Andrey Efimov at Fox Chase Cancer Center for providing us with lentiviral constructs.

This work was supported by National Institutes of Health grants GM095977 (T.M. Svitkina), GM110155 (J.E. Bear), and HL115553 (R.K. Assoian) and National Science Foundation Science and Technology Center for Engineering Mechanobiology award CMMI-1548571 (S. Talwar).

The authors declare no competing financial interests.

Author contributions: M.S. Shutova and T.M. Svitkina conceived the project, designed research, and wrote the paper. M.S. Shutova performed the majority of experiments and analyzed the data. S.B. Asokan and J.E. Bear designed and performed chemotaxis assays and analyzed the data. S. Talwar and R.K. Assoian designed and performed traction force microscopy experiments and analyzed the data.

Submitted: 24 May 2017
Revised: 16 June 2017
Accepted: 20 June 2017

References

Applewhite, D.A., M. Barzik, S. Kojima, T.M. Svitkina, F.B. Gertler, and G.G. Borisy. 2007. Ena/VASP proteins have an anti-capping independent function in filopodia formation. *Mol. Biol. Cell.* 18:2579–2591. http://dx.doi.org/10.1091/mbc.E06-11-0990

Asokan, S.B., H.E. Johnson, A. Rahman, S.J. King, J.D. Rotty, I.P. Lebedeva, J.M. Haugh, and J.E. Bear. 2014. Mesenchymal chemotaxis requires selective inactivation of myosin II at the leading edge via a noncanonical PLCγ/PKCα pathway. *Dev. Cell.* 31:747–760. http://dx.doi.org/10.1016/j.devcel.2014.10.024

Bao, J., S.S. Jana, and R.S. Adelstein. 2005. Vertebrate nonmuscle myosin II isoforms rescue small interfering RNA-induced defects in COS-7 cell cytokinesis. *J. Biol. Chem.* 280:19594–19599. http://dx.doi.org/10.1074/jbc.M501573200

Beach, J.R., and J.A. Hammer III. 2015. Myosin II isoform co-assembly and differential regulation in mammalian systems. *Exp. Cell Res.* 334:2–9. http://dx.doi.org/10.1016/j.yexcr.2015.01.012

Beach, J.R., L. Shao, K. Remmert, D. Li, E. Betzig, and J.A. Hammer III. 2014. Nonmuscle myosin II isoforms coassemble in living cells. *Curr. Biol.* 24:1160–1166. (published erratum appears in *Curr. Biol.* 2015. 25:402.) http://dx.doi.org/10.1016/j.cub.2014.03.071

Betapudi, V. 2010. Myosin II motor proteins with different functions determine the fate of lamellipodia extension during cell spreading. *PLoS One.* 5:e8560. http://dx.doi.org/10.1371/journal.pone.0008560

Betapudi, V., L.S. Licate, and T.T. Egelhoff. 2006. Distinct roles of nonmuscle myosin II isoforms in the regulation of MDA-MB-231 breast cancer cell spreading and migration. *Cancer Res.* 66:4725–4733. http://dx.doi.org/10.1158/0008-5472.CAN-05-4236

Billington, N., A. Wang, J. Mao, R.S. Adelstein, and J.R. Sellers. 2013. Characterization of three full-length human nonmuscle myosin II paralogs. *J. Biol. Chem.* 288:33398–33410. http://dx.doi.org/10.1074/jbc.M113.499848

Burnette, D.T., L. Shao, C. Ott, A.M. Pasapera, R.S. Fischer, M.A. Baird, C. Der Loughian, H. Delanoe-Ayari, M.J. Paszek, M.W. Davidson, et al. 2014. A contractile and counterbalancing adhesion system controls the 3D shape of crawling cells. *J. Cell Biol.* 205:83–96. http://dx.doi.org/10.1083/jcb.201311104

Cai, Y., N. Biais, G. Giannone, M. Tanase, G. Jiang, J.M. Hofman, C.H. Wiggins, P. Silberzan, A. Buguin, B. Ladoux, and M.P. Sheetz. 2006. Nonmuscle myosin IIA-dependent force inhibits cell spreading and drives F-actin flow. *Biophys. J.* 91:3907–3920. http://dx.doi.org/10.1529/biophysj.106.084806

Cretu, A., P. Castagnino, and R. Assoian. 2010. Studying the effects of matrix stiffness on cellular function using acrylamide-based hydrogels. *J. Vis. Exp.* (42):2089.

Dembo, M., and Y.L. Wang. 1999. Stresses at the cell-to-substrate interface during locomotion of fibroblasts. *Biophys. J.* 76:2307–2316. http://dx.doi.org/10.1016/S0006-3495(99)77386-8

Doyle, A.D., M.L. Kutys, M.A. Conti, K. Matsumoto, R.S. Adelstein, and K.M. Yamada. 2012. Micro-environmental control of cell migration: Myosin IIA is required for efficient migration in fibrillar environments through control of cell adhesion dynamics. *J. Cell Sci.* 125:2244–2256. http://dx.doi.org/10.1242/jcs.098806

Dulyaninova, N.G., and A.R. Bresnick. 2013. The heavy chain has its day: Regulation of myosin-II assembly. *BioArchitecture.* 3:77–85. http://dx.doi.org/10.4161/bioa.26133

Dulyaninova, N.G., R.P. House, V. Betapudi, and A.R. Bresnick. 2007. Myosin-IIA heavy-chain phosphorylation regulates the motility of MDA-MB-231 carcinoma cells. *Mol. Biol. Cell.* 18:3144–3155. http://dx.doi.org/10.1091/mbc.E06-11-1056

Even-Ram, S., A.D. Doyle, M.A. Conti, K. Matsumoto, R.S. Adelstein, and K.M. Yamada. 2007. Myosin IIA regulates cell motility and actomyosin-microtubule crosstalk. *Nat. Cell Biol.* 9:299–309. http://dx.doi.org/10.1038/ncb1540

Golomb, E., X. Ma, S.S. Jana, Y.A. Preston, S. Kawamoto, N.G. Shoham, E. Goldin, M.A. Conti, J.R. Sellers, and R.S. Adelstein. 2004. Identification and characterization of nonmuscle myosin II-C, a new member of the myosin II family. *J. Biol. Chem.* 279:2800–2808. http://dx.doi.org/10.1074/jbc.M309981200

Heissler, S.M., and D.J. Manstein. 2013. Nonmuscle myosin-2: Mix and match. *Cell. Mol. Life Sci.* 70:1–21. http://dx.doi.org/10.1007/s00018-012-1002-9

Heissler, S.M., and J.R. Sellers. 2016. Kinetic adaptations of myosins for their diverse cellular functions. *Traffic.* 17:839–859. http://dx.doi.org/10.1111/tra.12388

Hotulainen, P., and P. Lappalainen. 2006. Stress fibers are generated by two distinct actin assembly mechanisms in motile cells. *J. Cell Biol.* 173:383–394. http://dx.doi.org/10.1083/jcb.200511093

Jorrisch, M.H., W. Shih, and S. Yamada. 2013. Myosin IIA deficient cells migrate efficiently despite reduced traction forces at cell periphery. *Biol. Open.* 2:368–372. http://dx.doi.org/10.1242/bio.20133707

Juanes-Garcia, A., J.R. Chapman, R. Aguilar-Cuenca, C. Delgado-Arevalo, J. Hodges, L.A. Whitmore, J. Shabanowitz, D.F. Hunt, A.R. Horwitz, and M. Vicente-Manzanares. 2015. A regulatory motif in nonmuscle myosin II-B regulates its role in migratory front-back polarity. *J. Cell Biol.* 209:23–32. http://dx.doi.org/10.1083/jcb.201407059

Kelley, C.A., J.R. Sellers, D.L. Gard, D. Bui, R.S. Adelstein, and I.C. Baines. 1996. *Xenopus* nonmuscle myosin heavy chain isoforms have different subcellular localizations and enzymatic activities. *J. Cell Biol.* 134:675–687. (published erratum appears in *J. Cell Biol.* 1997. 138:215) http://dx.doi.org/10.1083/jcb.134.3.675

Kim, J.H., and R.S. Adelstein. 2011. LPA(1) -induced migration requires nonmuscle myosin II light chain phosphorylation in breast cancer cells. *J. Cell. Physiol.* 226:2881–2893. http://dx.doi.org/10.1002/jcp.22631

Kolega, J. 1998. Cytoplasmic dynamics of myosin IIA and IIB: Spatial 'sorting' of isoforms in locomoting cells. *J. Cell Sci.* 111:2085–2095.

Kovac, B., J.L. Teo, T.P. Mäkelä, and T. Vallenius. 2013. Assembly of non-contractile dorsal stress fibers requires α-actinin-1 and Rac1 in migrating and spreading cells. *J. Cell Sci.* 126:263–273. http://dx.doi.org/10.1242/jcs.115063

Kovács, M., K. Thirumurugan, P.J. Knight, and J.R. Sellers. 2007. Load-dependent mechanism of nonmuscle myosin 2. *Proc. Natl. Acad. Sci. USA.* 104:9994–9999. http://dx.doi.org/10.1073/pnas.0701181104

Lo, C.M., D.B. Buxton, G.C. Chua, M. Dembo, R.S. Adelstein, and Y.L. Wang. 2004. Nonmuscle myosin IIb is involved in the guidance of fibroblast migration. *Mol. Biol. Cell.* 15:982–989. http://dx.doi.org/10.1091/mbc.E03-06-0359

Maupin, P., C.L. Phillips, R.S. Adelstein, and T.D. Pollard. 1994. Differential localization of myosin-II isozymes in human cultured cells and blood cells. *J. Cell Sci.* 107:3077–3090.

Nagy, A., Y. Takagi, N. Billington, S.A. Sun, D.K. Hong, E. Homsher, A. Wang, and J.R. Sellers. 2013. Kinetic characterization of nonmuscle myosin IIb at the single molecule level. *J. Biol. Chem.* 288:709–722. http://dx.doi.org/10.1074/jbc.M112.424671

Nakasawa, T., M. Takahashi, F. Matsuzawa, S. Aikawa, Y. Togashi, T. Saitoh, A. Yamagishi, and M. Yazawa. 2005. Critical regions for assembly of vertebrate nonmuscle myosin II. *Biochemistry.* 44:174–183. http://dx.doi.org/10.1021/bi048807h

Raab, M., J. Swift, P.C. Dingal, P. Shah, J.W. Shin, and D.E. Discher. 2012. Crawling from soft to stiff matrix polarizes the cytoskeleton and phosphoregulates myosin-II heavy chain. *J. Cell Biol.* 199:669–683. http://dx.doi.org/10.1083/jcb.201205056

Ricketson, D., C.A. Johnston, and K.E. Prehoda. 2010. Multiple tail domain interactions stabilize nonmuscle myosin II bipolar filaments. *Proc. Natl. Acad. Sci. USA.* 107:20964–20969. http://dx.doi.org/10.1073/pnas.1007025107

Saitoh, T., S. Takemura, K. Ueda, H. Hosoya, M. Nagayama, H. Haga, K. Kawabata, A. Yamagishi, and M. Takahashi. 2001. Differential localization of non-muscle myosin II isoforms and phosphorylated regulatory light chains in human MRC-5 fibroblasts. *FEBS Lett.* 509:365–369. http://dx.doi.org/10.1016/S0014-5793(01)03186-6

Sandquist, J.C., and A.R. Means. 2008. The C-terminal tail region of nonmuscle myosin II directs isoform-specific distribution in migrating cells. *Mol. Biol. Cell.* 19:5156–5167. http://dx.doi.org/10.1091/mbc.E08-05-0533

Sandquist, J.C., K.I. Swenson, K.A. Demali, K. Burridge, and A.R. Means. 2006. Rho kinase differentially regulates phosphorylation of nonmuscle myosin II isoforms A and B during cell rounding and migration. *J. Biol. Chem.* 281:35873–35883. http://dx.doi.org/10.1074/jbc.M605343200

Schulze, N., M. Graessl, A. Blancke Soares, M. Geyer, L. Dehmelt, and P. Nalbant. 2014. FHOD1 regulates stress fiber organization by controlling the dynamics of transverse arcs and dorsal fibers. *J. Cell Sci.* 127:1379–1393. http://dx.doi.org/10.1242/jcs.134627

Shih, W., and S. Yamada. 2010. Myosin IIA dependent retrograde flow drives 3D cell migration. *Biophys. J.* 98:L29–L31. http://dx.doi.org/10.1016/j.bpj.2010.02.028

Shutova, M.S., W.A. Spessott, C.G. Giraudo, and T. Svitkina. 2014. Endogenous species of mammalian nonmuscle myosin IIA and IIB include activated monomers and heteropolymers. *Curr. Biol.* 24:1958–1968. http://dx.doi.org/10.1016/j.cub.2014.07.070

Small, J.V., K. Rottner, I. Kaverina, and K.I. Anderson. 1998. Assembling an actin cytoskeleton for cell attachment and movement. *Biochim. Biophys. Acta.* 1404:271–281. http://dx.doi.org/10.1016/S0167-4889(98)00080-9

Smalley-Freed, W.G., A. Efimov, P.E. Burnett, S.P. Short, M.A. Davis, D.L. Gumucio, M.K. Washington, R.J. Coffey, and A.B. Reynolds. 2010. p120-catenin is essential for maintenance of barrier function and intestinal homeostasis in mice. *J. Clin. Invest.* 120:1824–1835. http://dx.doi.org/10.1172/JCI41414

Soiné, J.R., C.A. Brand, J. Stricker, P.W. Oakes, M.L. Gardel, and U.S. Schwarz. 2015. Model-based traction force microscopy reveals differential tension in cellular actin bundles. *PLOS Comput. Biol.* 11:e1004076. http://dx.doi.org/10.1371/journal.pcbi.1004076

Thomas, D.G., A. Yenepalli, C.M. Denais, A. Rape, J.R. Beach, Y.L. Wang, W.P. Schiemann, H. Baskaran, J. Lammerding, and T.T. Egelhoff. 2015. Non-muscle myosin IIB is critical for nuclear translocation during 3D invasion. *J. Cell Biol.* 210:583–594. http://dx.doi.org/10.1083/jcb.201502039

Tojkander, S., G. Gateva, and P. Lappalainen. 2012. Actin stress fibers: Assembly, dynamics and biological roles. *J. Cell Sci.* 125:1855–1864. http://dx.doi.org/10.1242/jcs.098087

Tojkander, S., G. Gateva, A. Husain, R. Krishnan, and P. Lappalainen. 2015. Generation of contractile actomyosin bundles depends on mechanosensitive actin filament assembly and disassembly. *eLife.* 4:e06126. http://dx.doi.org/10.7554/eLife.06126

Tseng, Q., E. Duchemin-Pelletier, A. Deshiere, M. Balland, H. Guillou, O. Filhol, and M. Théry. 2012. Spatial organization of the extracellular matrix regulates cell-cell junction positioning. *Proc. Natl. Acad. Sci. USA.* 109:1506–1511. http://dx.doi.org/10.1073/pnas.1106377109

Verkhovsky, A.B., T.M. Svitkina, and G.G. Borisy. 1995. Myosin II filament assemblies in the active lamella of fibroblasts: their morphogenesis and role in the formation of actin filament bundles. *J. Cell Biol.* 131:989–1002. http://dx.doi.org/10.1083/jcb.131.4.989

Vicente-Manzanares, M., J. Zareno, L. Whitmore, C.K. Choi, and A.F. Horwitz. 2007. Regulation of protrusion, adhesion dynamics, and polarity by myosins IIA and IIB in migrating cells. *J. Cell Biol.* 176:573–580. (published erratum appears in *J. Cell Biol.* 2007. 176:1073) http://dx.doi.org/10.1083/jcb.200612043

Vicente-Manzanares, M., M.A. Koach, L. Whitmore, M.L. Lamers, and A.F. Horwitz. 2008. Segregation and activation of myosin IIB creates a rear in migrating cells. *J. Cell Biol.* 183:543–554. http://dx.doi.org/10.1083/jcb.200806030

Vicente-Manzanares, M., K. Newell-Litwa, A.I. Bachir, L.A. Whitmore, and A.R. Horwitz. 2011. Myosin IIA/IIB restrict adhesive and protrusive signaling to generate front-back polarity in migrating cells. *J. Cell Biol.* 193:381–396. http://dx.doi.org/10.1083/jcb.201012159

Wang, A., X. Ma, M.A. Conti, and R.S. Adelstein. 2011. Distinct and redundant roles of the non-muscle myosin II isoforms and functional domains. *Biochem. Soc. Trans.* 39:1131–1135. http://dx.doi.org/10.1042/BST0391131

Wei, Q., and R.S. Adelstein. 2000. Conditional expression of a truncated fragment of nonmuscle myosin II-A alters cell shape but not cytokinesis in HeLa cells. *Mol. Biol. Cell.* 11:3617–3627. http://dx.doi.org/10.1091/mbc.11.10.3617

Wu, C., S.B. Asokan, M.E. Berginski, E.M. Haynes, N.E. Sharpless, J.D. Griffith, S.M. Gomez, and J.E. Bear. 2012. Arp2/3 is critical for lamellipodia and response to extracellular matrix cues but is dispensable for chemotaxis. *Cell.* 148:973–987. http://dx.doi.org/10.1016/j.cell.2011.12.034